

Mass enhancement, correlations, and strong-coupling superconductivity in the β -pyrochlore KOs_2O_6

M. Brühwiler,* S. M. Kazakov, J. Karpinski, and B. Batlogg

Laboratory for Solid State Physics, ETH Zürich, 8093 Zürich, Switzerland

(Received 21 December 2005; revised manuscript received 17 February 2006; published 30 March 2006)

To assess electron correlation and electron-phonon coupling in the recently discovered β -pyrochlores KOs_2O_6 and RbOs_2O_6 , we have performed specific heat measurements in magnetic fields up to 14 T. We present data from high-quality single-crystalline KOs_2O_6 , showing that KOs_2O_6 is a strong-coupling superconductor with a coupling parameter $\lambda_{\text{ep}} \approx 1.0$ – 1.6 (RbOs_2O_6 : $\lambda_{\text{ep}} \approx 1$). The estimated Sommerfeld coefficient of KOs_2O_6 , $\gamma = 76$ – 110 mJ/mol K², is twice that of RbOs_2O_6 ($\gamma = 44$ mJ/mol K²). Using strong-coupling corrections, we extract useful thermodynamic parameters of KOs_2O_6 . Quantifying λ_{ep} allows us to determine the mass enhancement over the calculated band electronic density of states. A significant contribution in addition to the electron-phonon term of $\lambda_{\text{c}} = 1.7$ – 4.3 is deduced. In an effort to understand the origin of the enhancement mechanism, we also investigate an unusual energetically low-lying phonon. There are three phonon modes per RbOs_2O_6 , suggestive of the phonon source being the rattling motion of the alkali-metal ion. This dynamic instability of the alkali-metal ions causes large scattering of the charge carriers which shows up in an unusual temperature dependence of the electrical resistivity.

DOI: [10.1103/PhysRevB.73.094518](https://doi.org/10.1103/PhysRevB.73.094518)

PACS number(s): 74.25.Bt, 74.25.Op, 74.70.–b

I. INTRODUCTION

Long-standing interest in the pyrochlores stems from their inherent geometrical frustration due to the metal ions forming a network of corner-sharing tetrahedra. For insulating pyrochlores, where localized magnetic moments sit on the vertices of these tetrahedra, competing interactions lead to a wealth of states of fundamental interest. Ground states of infinite degeneracy are a typical signature of such frustrated systems.^{1–3} While for insulating systems the intimate connection between spins and the lattice topology leads to the observed frustration effects, it is an open question how charge, spin, and lattice degrees of freedom are coupled in itinerant systems and how they influence each other.

In this context, the superconductivity recently found in KOs_2O_6 has been of considerable interest.⁴ It has been thought that a spin liquid ground state resulting from frustration in these structures might favor superconductivity through singlet pairing by a resonating valence bond.⁵ At the time of its discovery, KOs_2O_6 was the second pyrochlore superconductor known after $\text{Cd}_2\text{Re}_2\text{O}_7$.^{6–8} Soon after, the discovery of superconducting RbOs_2O_6 (Refs. 9 and 10) and CsOs_2O_6 (Ref. 11) followed. $\text{Cd}_2\text{Re}_2\text{O}_7$ crystallizes in the so-called α -pyrochlore structure, the structure adopted by numerous insulating pyrochlores, and AOs_2O_6 (where $A = \text{Cs}$, Rb , or K) has the β -pyrochlore structure. While the AOs_2O_6 compounds could be expected to be very similar in their physical properties, there is in fact quite a variation among them.

For example, T_c decreases from 9.5 K for KOs_2O_6 to 6.4 K for RbOs_2O_6 and to 3.3 K for CsOs_2O_6 . The nature of the superconducting state is still under discussion: while RbOs_2O_6 appears to be a fully gapped s -wave superconductor with a critical temperature $T_c = 6.4$ K,^{12–16} muon spin resonance (μSR) measurements point toward an anisotropic or multigapped superconducting state in KOs_2O_6 .¹⁷ This

question has not been settled conclusively. It has been found that KOs_2O_6 single crystals show Bragg peaks that violate the $Fd\bar{3}m$ symmetry and the structure has been identified as noncentrosymmetric $F\bar{4}3m$.¹⁸ Furthermore, it remains to be determined to what degree the quasiparticle mass is enhanced by interactions other than those with ordinary phonons, e.g., to what extent electron-electron correlations play a role in these compounds. In order to address these questions a detailed characterization of these compounds is required.

In this paper, we present field- and temperature-dependent thermodynamic and transport measurements on RbOs_2O_6 and KOs_2O_6 . The data provide evidence for a significant additional electronic mass enhancement beyond the contribution from the coupling to phonons and evidence for low-lying vibrational modes. We discuss similarities and differences between the two compounds and compile an extended list of the basic thermodynamic parameters.

II. EXPERIMENT

KOs_2O_6 single crystals have been grown by an encapsulation technique in an evacuated quartz tube. In this method, a stoichiometric amount of Os metal (Alfa Aesar, 99.9%) and KO_2 (Alfa Aesar, 95%) is thoroughly mixed in an argon-filled dry box and pressed into a pellet. The pellet with a mass of 0.2–0.25 g is put into a quartz tube and silver oxide Ag_2O (Aldrich, 99%) is added to create an appropriate oxygen partial pressure during the synthesis. The evacuated and sealed tube is then inserted into a furnace preheated to 600 °C, kept there for 1 h, cooled to 400 °C at a rate of 5 °C/h, and then cooled to room temperature at a rate of 150 °C/h. The resulting black single crystals of size up to 0.3 mm in diameter have grown on the wall of the quartz tube and on the surface of the precursor pellet. The crystals

have different shapes characteristic for the cubic structure such as octahedra or cubes. The lattice parameter refined from x-ray single-crystal measurements is found to be $a = 10.0968(8)$ Å. No signature of impurity phases like OsO_2 or KO_2 was found in heat capacity and magnetization measurements.

For the specific heat measurements, we have selected about five dozen of the most regularly shaped single crystals out of a single badge. The total mass of these crystals amounts to 2.12 mg (see inset to Fig. 2), which is enough to measure specific heat with a relaxation method. Special attention must be paid, however, to measuring the addendum contribution as it makes up a significant fraction of the total mass. The specific heat has been measured in a physical properties measurement apparatus using an adiabatic relaxation technique (Quantum Design, PPMS). Resistivity has been measured by a standard four-terminal approach also using the PPMS and the dc magnetization has been measured in a superconducting quantum interference device magnetometer (Quantum Design, MPMS). Measurements on RbOs_2O_6 have been performed on a sample previously reported upon in Ref. 15. The synthesis procedure of these polycrystalline RbOs_2O_6 samples is described elsewhere.^{4,19}

III. RESULTS

In order to determine the mass enhancement in the normal state and the magnitude of the electron-phonon coupling, it is necessary to measure the Sommerfeld coefficient of the superconductor by driving it into the normal state. Usually this is achieved by applying a magnetic field exceeding the upper critical field H_{c2} . Owing to a high $H_{c2}(0 \text{ K})$ of KO_2O_6 which is inaccessible by our 14 T magnet, it is not possible to tune KO_2O_6 into its normal state below about 6.2 K. We therefore resort to an extrapolation method to estimate the Sommerfeld coefficient. First we measure the phase boundary line $H_{c2}(T)$ to as low a temperature and high field as possible. We then extrapolate H_{c2} to 0 K and estimate the Sommerfeld coefficient based on the measured C_p/T versus magnetic field curve at a low temperature. The details of this procedure are given in the following.

A. Upper critical field H_{c2}

We extract the upper critical field H_{c2} from $C_p(T)$ data for KO_2O_6 and from both $C_p(T)$ and $C_p(H)$ data for RbOs_2O_6 . For both methods, we use a construction of equal area to determine the critical field. The two methods result in almost identical H_{c2} as can be seen in Fig. 1. In our experience, the H_{c2} slope at T_c for both RbOs_2O_6 and KO_2O_6 are rather stable quantities varying little from sample to sample. We therefore have a high level of confidence that the observed slope is indeed intrinsic to the material and not mainly limited by a mean free path caused by impurity scattering.

The initial slope of the critical boundary at T_c for KO_2O_6 is -3.6 T/K , in agreement with the revised value in Refs. 10 and 20. The full $H_{c2}(T)$ dependence cannot be mapped out with the 14 T magnet, so we need to extrapolate to lower temperatures and we proceed in two different ways. First, we

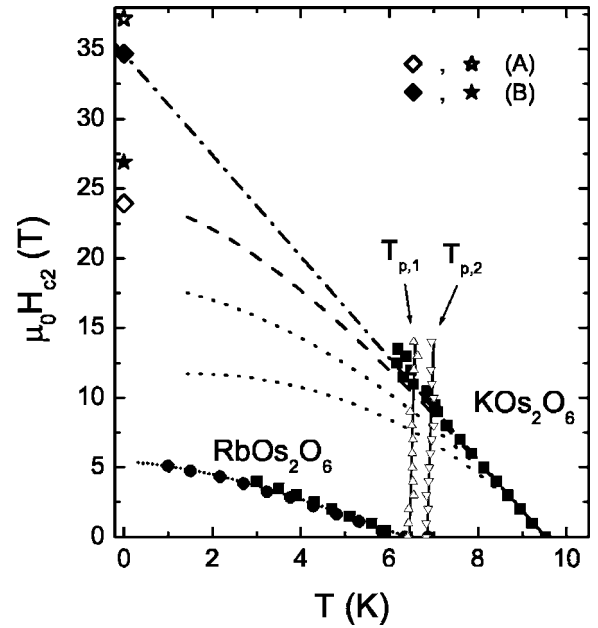


FIG. 1. The upper critical field $H_{c2}(T)$ of KO_2O_6 and RbOs_2O_6 . The squares (■) are data points extracted from C_p/T versus T data, while the circles (●) are extracted from C_p/T versus H data. For KO_2O_6 , two methods to extrapolate to 0 K are used. (A) The dashed line is from the WHH formula in the orbital limit ($\lambda_{\text{SO}} = \infty$), providing a good description of the data up to about 9 T, while a description with smaller spin-orbit scattering strength (dotted lines) deviates markedly. (B) The dash-dotted line is a linear fit to the data. The stars mark the Pauli limiting field $\mu_0 H_P$ for KO_2O_6 . $T_{p,1}$ and $T_{p,2}$ mark two additional peaks observed in the specific heat (Fig. 3) that might be associated with K ordering.

notice that $H_{c2}(T)$ in RbOs_2O_6 is rather well described by the standard Werthamer-Helfand-Hohenberg (WHH) expression, with an initial slope of -1.2 T/K and $\mu_0 H_{c2}(0 \text{ K}) = 6 \text{ T}$ (Fig. 1).¹² If we were to assume the same functional form to hold also for KO_2O_6 , $\mu_0 H_{c2}(0 \text{ K}) = 24 \text{ T}$ is estimated. Considering that a typical energy of low-lying phonons in KO_2O_6 is around 30 K, H_{c2} might be underestimated in this way. Alternatively, one can extrapolate linearly to $T = 0 \text{ K}$ and would estimate $\mu_0 H_{c2}(0 \text{ K}) = 35 \text{ T}$. Pursuing this second extrapolation further is motivated by our observation that the last data points in our data lie closer to a straight line extrapolation of the lower-field data, while the WHH curve starts deviating from the data in this region. In the rest of this paper, we thus consider both extrapolations, denoting with (A) the WHH version, and with (B) the linear method. Numerical values for (B) will be enclosed in braces { }.

It is worth noting that the RbOs_2O_6 and KO_2O_6 data are fitted best by the WHH formula in the orbital limit ($\lambda_{\text{SO}} = \infty$). This is in agreement with a large λ_{SO} expected for the heavy Os ion. Therefore, pair-breaking effects of the magnetic field on the spin degrees of freedom are negligible due to the randomizing effect of the spin-orbit scattering on the phase of the superconducting electrons. An upper limit of the critical field in the case where spin-orbit scattering could be ignored is given by the Pauli limiting field: for KO_2O_6 it is $\mu_0 H_P = \Delta(0 \text{ K}) / (\sqrt{2} \mu_B) \sqrt{1 + \lambda_{\text{ep}}} \approx 37 \text{ T}$ {27 T}, while for

TABLE I. Thermodynamic parameters of the superconductors KOs_2O_6 and RbOs_2O_6 .

Parameter	KOs_2O_6	RbOs_2O_6
T_c	9.5 K	6.4 K
$\xi(0 \text{ K})$	37 Å {31 Å}	74 Å
$\lambda_{\text{eff}}(0 \text{ K})$	243 nm {265 nm}	252 nm
$\kappa(T_c), \kappa(0 \text{ K})$	45, 66 {45, 86}	23, 34
γ	76 {110} mJ/(mol _{f.u.} K ²)	44 mJ/(mol _{f.u.} K ²)
$\Delta C_p _{T_c}/(\gamma T_c)$	2.7 {1.9}	1.9
λ_{ep}	1.6 {1.0}	1.0
λ_c	1.7 {4.3}	1.0
b	0.95 K ⁻¹ {0.77 K ⁻¹ }	1.12 K ⁻¹
b/T_c	0.099 K ⁻² {0.080 K ⁻² }	0.175 K ⁻²
bT_c	9.021 {7.299}	7.168
$-\Delta F(0 \text{ K})$	2050 {2533} mJ/mol _{f.u.}	483 mJ/mol _{f.u.}
$H_c(0 \text{ K})$	2579 Oe {2867 Oe}	1249 Oe
$H_{c1}(0 \text{ K})$	116 Oe {105 Oe}	92 Oe
$\mu_0 H_{c2}(0 \text{ K})$	24 T {35 T}	6 T
$-dH_c/dT _{T_c}$	575 Oe/K	369 Oe/K
$-d\mu_0 H_{c2}/dT _{T_c}$	3.6 T/K	1.2 T/K
$Q \equiv -2T_c/H_c(0) \times dH_c/dT _{T_c}$	4.25 {3.82}	3.79
$k_B T_c/(\hbar \omega_{\text{in}})$	0.13 {0.06}	0.06
$2\Delta(0 \text{ K})/(k_B T_c)$	4.57 {3.83}	3.87
$[1/(8\pi)]\gamma T_c^2/(-\Delta F)$	0.13 {0.16}	0.15

RbOs_2O_6 it is about 18 T. Here we have used the values for $\Delta(0 \text{ K})$ and λ_{ep} determined from our measurements as described later and listed in Table I. For RbOs_2O_6 , this field is well above the measured upper critical field, while for KOs_2O_6 the comparison depends on the extrapolation of H_{c2} . Support for the fact that H_{c2} is determined by the orbital motion of the electrons and not by their spin is provided by the ratio of the slopes $-d\mu_0 H_{c2}/dT|_{T_c}$ for the two materials RbOs_2O_6 and KOs_2O_6 . The slopes are proportional to $1/(\tau v_F^2)$, where τ is the electronic scattering time and v_F the Fermi velocity. For the Fermi velocities we use $2.587 \times 10^7 \text{ cm/s}$ for RbOs_2O_6 and $2.671 \times 10^7 \text{ cm/s}$ for KOs_2O_6 .²¹ The ratio of the Fermi velocities squared, taking into account the renormalization of the Fermi velocity and assuming the same τ for both materials, is 2.4 {4.7}. This is indeed close to the ratio of $-d\mu_0 H_{c2}/dT|_{T_c}$ for RbOs_2O_6 and KOs_2O_6 , 3.6/1.2=3, suggesting that the pair breaking is caused conventionally by the effect of the magnetic field on the orbital magnetism of the electrons. The difference in magnitude of the upper critical fields is therefore in line with the different mass enhancements.

B. Heat capacity in a magnetic field

We have measured the field dependence of C_p/T of KOs_2O_6 at 0.46 K, shown in Fig. 2. The addendum is $\approx 10\%$ of the total heat capacity at $\mu_0 H = 14 \text{ T}$, $\approx 20\%$ at $\mu_0 H = 7 \text{ T}$, and $\approx 50\%$ at $\mu_0 H = 3 \text{ T}$. Below $\mu_0 H = 1.7 \text{ T}$, the addendum makes up more than 90% of the total heat capacity, and even though both data sets are very smooth, this leads to

relatively larger scatter after taking the difference of the two data sets. For this reason, data below 1.7 T have been omitted in the graph and in the fitting procedure.

We parametrize the measured curve by $C_p/T = a[H \text{ (Oe)}]^b + c$. A least-squares fit down to 1.75 T using this

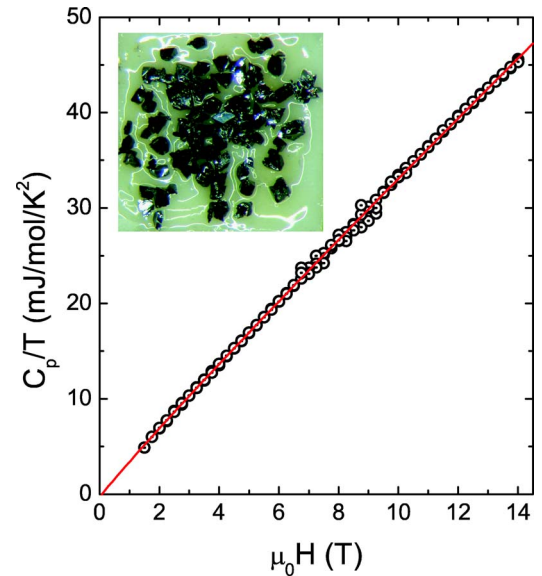


FIG. 2. (Color online) Heat capacity versus magnetic field of KOs_2O_6 at 0.46 K. An extrapolation to the upper critical field $H_{c2} \approx 24 \text{ T}$ {35 T} results in a Sommerfeld coefficient $\gamma = 76 \text{ mJ/mol K}^2$ { $\gamma = 110 \text{ mJ/mol K}^2$ }. The inset shows the measured crystals.

form results in $a=(5.86\pm 1.3)\times 10^{-4}$ mJ/mol K², $b=0.9512\pm 0.02$, and $c=-0.35\pm 0.4$ mJ/mol K², where H is given in oersteds. An extrapolation of the $C_p(H)$ curve at 0.46 K to the upper critical field H_{c2} of 24 T {35 T} results in a rather high Sommerfeld coefficient for KOs_2O_6 of $\gamma=76$ mJ/mol K² {110 mJ/mol K²}.

The fact that we have measured a vanishingly small C_p/T at $H=0$ Oe and $T=0.46$ K is of significance for the interpretation of the electronic and vibrational excitation spectrum. First, it indicates that the superconducting state affects the entire electronic system that gives rise to the large γ value (76–110 mJ/mol K²). Second, the vibrational excitation spectrum (at 0.46 K) is not characterized by a glasslike spectrum ($C_p \propto T$) as one might expect from a broad distribution of two-level configurations possibly associated with the particular lattice potential experienced by the K ions.²²

In addition to estimating the Sommerfeld coefficient, measurements of the magnetic-field-dependent heat capacity can be helpful to reveal nodes in the gap function. It is generally thought that a square root dependence $C_p/T \propto H^\alpha$ with $\alpha=1/2$ indicates a gap with nodes, while a linear dependence $\alpha=1$ indicates a fully gapped state.²³ This is because the electronic excitations in the vortex state of conventional superconductors are predominantly low-energy excitations localized in the vortex core. On the other hand, the density of states for superconductors with lines of gap nodes results mostly from delocalized states outside the vortex which are located in the vicinity of the gap nodes in momentum space.

We expect that the exponent in the above fit to C_p versus H tends even closer toward 1 as $T \rightarrow 0$ K, since the exponent decreases when measuring at increasingly higher temperatures (data not shown). The field dependence of the heat capacity of KOs_2O_6 thus appears to be in line with a fully gapped state. However, since the measurements do not extend up to H_{c2} , further experimental evidence is needed to settle this point conclusively.

C. Density of states and mass enhancement

The specific heat for KOs_2O_6 in various fields is shown in Fig. 3. In addition to the anomaly indicating the transition into the superconducting state, there are two additional peaks at $T_{p,1}$ (≈ 6.5 K) and $T_{p,2}$ (≈ 7 K). The origin of these peaks is unclear at this point. They are likely to be associated with the dynamics of the potassium ions in this compound. While we measure two peaks for our sample, a single peak has been reported in Refs. 10 and 20 at a slightly higher temperature (about 7.5 K)—the transition seems to be very sensitive to microscopic details.

From the specific heat jump at T_c , $\Delta C_p|_{T_c}/T_c = 204$ mJ/mol K², the normalized specific heat jump $\Delta C_p|_{T_c}/(\gamma T_c) = 2.7$ {1.9} is extracted. It is significantly larger than in the weak-coupling limit and corresponds to an electron-phonon coupling constant $\lambda_{ep} = 2\int_0^\infty \alpha^2 F(\omega)/\omega d\omega \approx 1.6$ {1.0},²⁴ i.e., KOs_2O_6 is a superconductor in the strong-coupling regime. Here, $\alpha^2 F(\omega)$ is the spectral density of the electron-phonon coupling function. Using the calculated band Sommerfeld coefficient $\gamma_b = 9.8$ –11.36 mJ/mol K² of KOs_2O_6 from Refs. 22 and 25, this result indicates a signifi-

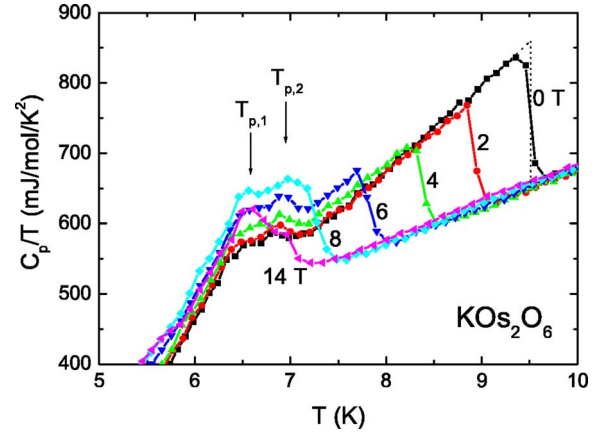


FIG. 3. (Color online) Heat capacity versus temperature of KOs_2O_6 for various magnetic fields. The specific heat jump at T_c , $\Delta C_p|_{T_c}/T_c$, is 204 mJ/mol K², from which the normalized specific heat jump $\Delta C_p|_{T_c}/(\gamma T_c) = 2.7$ {1.9} is extracted. It is significantly larger than that for the weak-coupling case and corresponds to an electron-phonon coupling constant $\lambda_{ep} \approx 1.0$ {1.6}, i.e., KOs_2O_6 is a superconductor in the strong-coupling regime. There are two transitions at $T_{p,1} \approx 6.5$ K and $T_{p,2} \approx 7$ K that might be associated with K ordering.

cant enhancement of the electronic specific heat of $(1 + \lambda_{ep}) \times (1 + \lambda_c) = (76 \text{ mJ/mol K}^2)/(10.6 \text{ mJ/mol K}^2) \approx 7.2$ {10.4}, i.e., about double the enhancement found in Sr_2RuO_4 of 3.8–4.^{26,27} This quantification of λ_{ep} then leaves a significant additional enhancement $\lambda_c \approx 1.7$ {4.3} ascribed to electron-electron correlations.

Figure 4 illustrates the density of states for KOs_2O_6 and RbOs_2O_6 and the weak-coupling α -pyrochlore superconductor $\text{Cd}_2\text{Re}_2\text{O}_7$ for comparison. The depicted band density of states for AOs_2O_6 is the arithmetic mean of the two calculated values in Refs. 22 and 25, and the values for $\text{Cd}_2\text{Re}_2\text{O}_7$ are taken from Refs. 6 and 28. It increases very slightly on going from $A=\text{K}$ to $A=\text{Rb}$ to $\text{Cd}_2\text{Re}_2\text{O}_7$, but is rather similar overall. The electronic structure in the local density approximation (LDA) as a whole is in fact very similar for all AOs_2O_6 . The electron-phonon enhancement, on the other hand varies significantly: λ_{ep} is less than about 0.4 for $\text{Cd}_2\text{Re}_2\text{O}_7$, but falls in the intermediate- to strong-coupling range for the osmates (1–1.6), indicating that there is a significant difference in the coupling functions leading to the superconducting state. The difference in the additional enhancement λ_c is pronounced: it increases more than twofold from RbOs_2O_6 to KOs_2O_6 , in the same direction as λ_{ep} .

To gain further insight into the mechanisms responsible for the density of states enhancement, it is helpful to consider the magnetic susceptibility (Fig. 5). Since samples of RbOs_2O_6 also contain some OsO_2 , the intrinsic magnetic susceptibility is calculated according to $\chi_1 = \eta_m^{-1} \chi - (\eta_m^{-1} - 1) \chi_2$, where χ_1 is the magnetic susceptibility of RbOs_2O_6 , χ_2 that of OsO_2 , and χ is the measured susceptibility of the mixed system (cf Sec. III E). The susceptibilities in this formula are given per mass. The correction due to OsO_2 is very small, since the susceptibility per Os is very similar in both systems. Even after taking into account the correction for OsO_2 , the susceptibility of RbOs_2O_6 still shows a slight in-

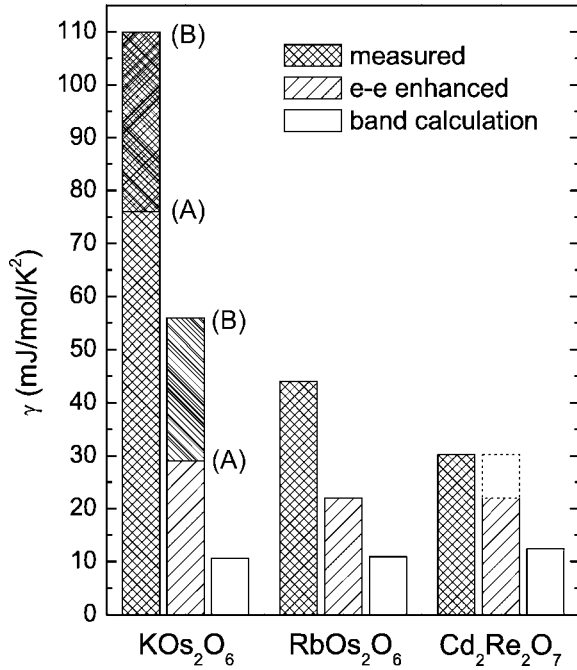


FIG. 4. Comparison of the Sommerfeld coefficients for RbOs₂O₆, KOs₂O₆, and the weak-coupling α -pyrochlore superconductor Cd₂Re₂O₇. Shown are the calculated bare coefficients γ_b in white, the electron-electron enhanced coefficients $(1+\lambda_c)\gamma_b$ in hatched, and the measured coefficients $(1+\lambda_{ep})(1+\lambda_c)\gamma_b$ in cross hatched. The bare band value from density functional theory calculations in the LDA is rather similar for all three pyrochlores. The electron-phonon coupling λ_{ep} increases from less than 0.4 (weak coupling) for Cd₂Re₂O₇ to 1 for RbOs₂O₆ to 1.0–1.6 for KOs₂O₆. The two sets of values (A) and (B) for KOs₂O₆ correspond to the two choices of extrapolating $H_{c2}(T)$ in Fig. 1.

crease at low temperatures and also a shoulder around 25 K. This is probably due to minute amounts of magnetic RbOs₄. We note that a similar T dependence as for the susceptibility has been observed for the Knight shift in both RbOs₂O₆ and KOs₂O₆.²⁹

We correct for the diamagnetism of the core using $\chi = \chi_{\text{exp}} - \chi_{\text{core}}$ with $\chi_{\text{core}} = -12, -20, -13$, and $-18 \mu\text{cm}^3/\text{mol}$ for O²⁻, Rb⁺, K⁺, and Os⁶⁺ ions, respectively. Landau diamagnetism can be neglected, due to the enhancement of the electron mass. For the experimental susceptibility, we use the value at 150 K, resulting in a susceptibility for KOs₂O₆ of $\chi^{\text{emu}} \approx 3.7 \times 10^{-4} \text{ cm}^3/\text{mol}$. The Sommerfeld-Wilson ratio evaluates to $R_W = 0.93 \text{ G}^2 \text{ cm}^3/\text{erg}$ [$0.65 \text{ G}^2 \text{ cm}^3/\text{erg}$] where we have used the renormalized Sommerfeld coefficient $\gamma/(1+\lambda_{ep})$ since the Pauli magnetic susceptibility is not affected by electron-phonon interactions. For RbOs₂O₆ follows $\chi^{\text{emu}} \approx 5.3 \times 10^{-4} \text{ cm}^3/\text{mol}$ and $R_W = 1.75 \text{ G}^2 \text{ cm}^3/\text{erg}$. In view of a calculated Stoner enhancement of the magnetic susceptibility of roughly 2 for all AOs₂O₆ (Refs. 22 and 25), the Wilson ratio for RbOs₂O₆ closely matches the expected result. On the other hand, R_W for KOs₂O₆ is clearly smaller than what would be expected. In this simple estimate, we have neglected possible orbital van Vleck terms that may also contribute to the paramagnetic susceptibility.

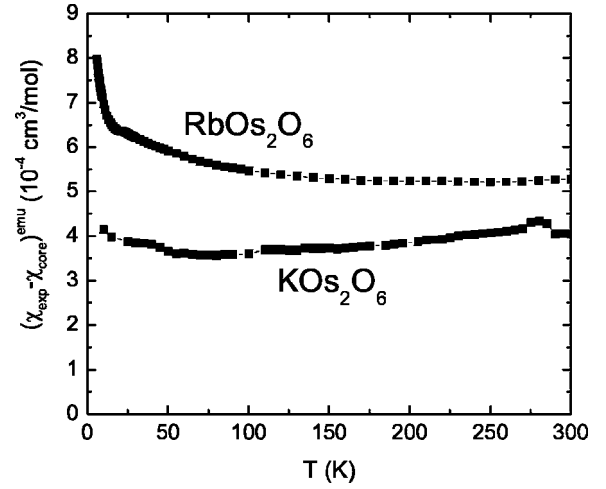


FIG. 5. Magnetic susceptibility of KOs₂O₆ and RbOs₂O₆ measured at 1 T. The data are corrected for the core diamagnetism ($+1.22 \times 10^{-4} \text{ cm}^3/\text{mol}$ for RbOs₂O₆, $+1.15 \times 10^{-4} \text{ cm}^3/\text{mol}$ for KOs₂O₆), resulting in susceptibilities taken at 150 K of $\chi^{\text{emu}} \approx 3.7 \times 10^{-4} \text{ cm}^3/\text{mol}$ for KOs₂O₆ and $\chi^{\text{emu}} \approx 5.3 \times 10^{-4} \text{ cm}^3/\text{mol}$ for RbOs₂O₆.

D. Superconducting properties

It is instructive to calculate the various thermodynamic parameters for KOs₂O₆ and RbOs₂O₆. We get a strong-coupling parameter $x := k_B T_c / (\hbar \omega_{\text{lin}}) = 0.13 \{0.06\}$ by applying the approximate semiphenomenological form of the strong-coupling correction to the weak-coupling BCS ratio which holds for many superconductors $\Delta C_p|_{T_c} / (\gamma T_c) = 1.43 [1 - 53x^2 \ln(3x)]$.³⁰ Here $\hbar \omega_{\text{lin}}$ is the Allen-Dynes expression for the average phonon energy. With this strong-coupling parameter we further get a normalized energy gap of $2\Delta(0 \text{ K}) / (k_B T_c) = 3.53 [1 - 12.5x^2 \ln(2x)] = 4.57 \{3.83\}$. Since we know from RbOs₂O₆ that another strong-coupling correction $[1/(8\pi)] \gamma T_c^2 / (-\Delta F) = 0.168 [1 + 12.2x^2 \ln(3x)]$, holds quite well,¹⁵ it is reasonable to assume that it also holds for KOs₂O₆. Using the experimental T_c , γ , and the strong-coupling parameter from above, we can estimate the condensation energy of KOs₂O₆: $-\Delta F = 2050 \text{ mJ/mol}$ [2533 mJ/mol], corresponding to a thermodynamic critical field of $H_c = 2579 \text{ Oe}$ [2867 Oe]. In this conversion we have used the calculated mass density of KOs₂O₆ using the lattice constant from x-ray diffraction, $\rho = 6.653 \text{ g/cm}^3$. The ratio $[1/(8\pi)] (\gamma T_c^2) / (-\Delta F)$ itself evaluates to 0.135 [0.157].

Once the condensation energy is known, various thermodynamic quantities can be evaluated: for $bT_c \equiv (T \Delta C_p)|_{T_c} / (-\Delta F)$ we get 9.02 [7.30], giving a normalized critical field slope $Q = 4.25 \{3.82\}$. The critical field slope itself evaluates to $-dH_c/dT|_{T_c} = 575 \text{ Oe/K}$. The slope of the upper critical field is about three times steeper than the one from RbOs₂O₆: with $-d\mu_0 H_{c2}/dT|_{T_c} = 3.6 \text{ T/K}$ (Fig. 1) we get a Ginzburg-Landau parameter at the critical temperature of $\kappa(T_c) = 45$. At $T \rightarrow 0 \text{ K}$, we estimate $\kappa(0 \text{ K}) = (1/\sqrt{2}) H_{c2}/H_c = 66 \{86\}$ and thus a penetration depth of 243 nm [265 nm], which compares well with results from μSR experiments (270 nm).¹⁷ The Ginzburg-Landau coherence length amounts to

$\xi=37 \text{ \AA}$ $\{31 \text{ \AA}\}$ and the lower critical field $H_{c1} = \ln \kappa / (\sqrt{2} \kappa) H_c = 116 \text{ Oe}$ $\{105 \text{ Oe}\}$. This lower critical field is in agreement with magnetization measurements (not shown). The Ginzburg-Landau coherence length is about half that of RbOs_2O_6 . The parameters are listed in Table I, where they are compared to the values of RbOs_2O_6 taken from Ref. 15 for convenience.

H_{c2} for KOs_2O_6 is beyond the 14 T accessible in our current setup, so that the samples cannot be tuned to the normal state below about 6.2 K. There is thus no reference measurement for the heat capacity in the normal state and the superconducting electronic specific heat C_{es} cannot be determined by a simple subtraction of a normal state and a superconducting state measurement. This renders determining additional contributions to the heat capacity other than the usual phononic and electronic terms difficult.

E. Unusual low-energy atomic vibrations

The specific heat of RbOs_2O_6 is analyzed using the condensation energy analysis (CEA) developed in Ref. 15. This is necessary because it is not yet possible to synthesize a fully phase-pure RbOs_2O_6 sample. OsO_2 has been identified by x-ray diffraction analysis as a secondary phase. This shortcoming is compensated by the fact that by using the CEA it is possible to extract the intrinsic properties of superconducting RbOs_2O_6 even if the samples contain some unreacted OsO_2 starting material.

The full temperature dependence of the intrinsic heat capacity of RbOs_2O_6 is therefore obtained by subtracting the appropriate amount of the OsO_2 heat capacity contribution according to $C_1 = \eta_m^{-1} C - (\gamma_m^{-1} - 1) C_2$. Here, C_1 is the heat capacity of RbOs_2O_6 , C_2 of OsO_2 , and C is the measured heat capacity of the mixed system, all in energy per temperature per mass. To this end we have measured a sample of the starting material OsO_2 . Its heat capacity is shown in Fig. 6 (C_2) together with the heat capacity of a RbOs_2O_6 sample (C) with a superconducting mass fraction of $\eta_m=74.9\%$. Hence, the difference between the mixed system heat capacity C and 25.1% of C_2 (shaded region) is 74.9% of the intrinsic heat capacity of RbOs_2O_6 C_1 . The Sommerfeld coefficients used in the plot are $\gamma=27.5 \text{ } \mu\text{J/g K}^2$ for OsO_2 and $\gamma=70.3 \text{ } \mu\text{J/g K}^2$ for the RbOs_2O_6 sample.

The resulting specific heat of RbOs_2O_6 (C_1) on a logarithmic temperature scale is shown in Fig. 7. In such a plot, an Einstein contribution to the heat capacity appears as a bell-shaped feature with a peak at $T=T_E/4.93$.³¹ The data clearly indicate such a contribution with an Einstein temperature of 60 K and a density of 0.33×9 modes/f.u. Assuming this phonon involves the displacement of the Rb atoms, this means an effective number of three modes per Rb ion. Three modes are compatible with a three-dimensional potential for the Rb ions to move in as is expected from the tetrahedral symmetry of the Rb site.

As the KOs_2O_6 samples are high-quality single crystals, the KOs_2O_6 data can be analyzed as measured. We have observed a vanishingly small residual Sommerfeld coefficient ($C_p/T \rightarrow -0.35 \pm 0.4 \text{ mJ/mol K}^2$ as $H \rightarrow 0 \text{ Oe}$ at 0.46 K) as expected from a single-phase sample and indica-

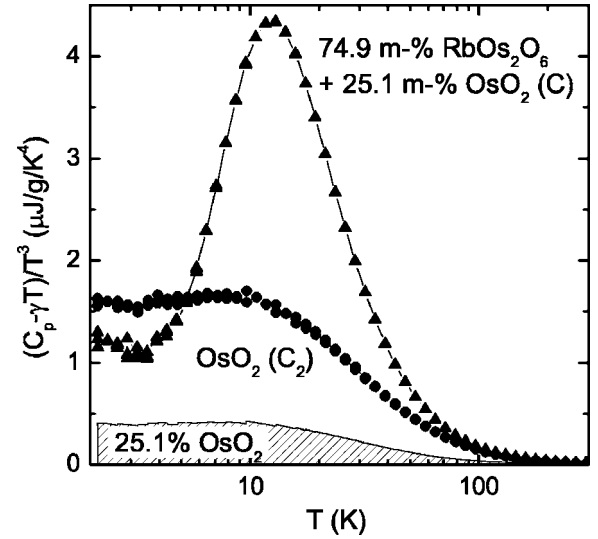


FIG. 6. $(C_p - \gamma T)/T^3$ versus temperature on a logarithmic scale of a RbOs_2O_6 sample with 74.9 mass % RbOs_2O_6 and 25.1 mass % OsO_2 and an OsO_2 sample. It illustrates the significant additional heat capacity present in RbOs_2O_6 . The difference between C and the shaded region is 74.9% of the intrinsic heat capacity of RbOs_2O_6 .

tive of a fully gapped electronic excitation spectrum. The temperature-dependent lattice heat capacity data are shown in Fig. 8. In the normal state above 6.2 K, γT was used for the electronic heat capacity C_{el} . The low-temperature data from 2 to 3.8 K were obtained using the electronic heat capacity of an isotropic superconductor $C_{el} = C_{es} = 8.5 \gamma T_c \times \exp[-1.44 \times 2\Delta(0 \text{ K})/3.53 \times T_c/T]$. The data do not fit as nicely to a combined Debye-Einstein model as do the data for RbOs_2O_6 . This might be due to the alkali-metal-ion po-

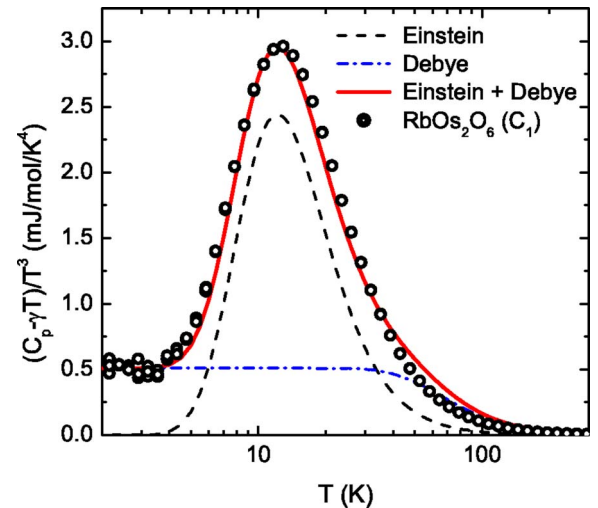


FIG. 7. (Color online) Decomposition of the lattice heat capacity $(C_p - \gamma T)/T^3$ of RbOs_2O_6 into Debye- and Einstein-mode components. In such a plot, an Einstein contribution to the heat capacity appears as a bell-shaped feature with a maximum at $T=T_E/4.93$ (Ref. 31). The data are well described by a combined Debye-Einstein model with $\Theta_D=325 \text{ K}$, $T_E=60 \text{ K}$, and $n \approx 0.33 \times 9$ modes per f.u.

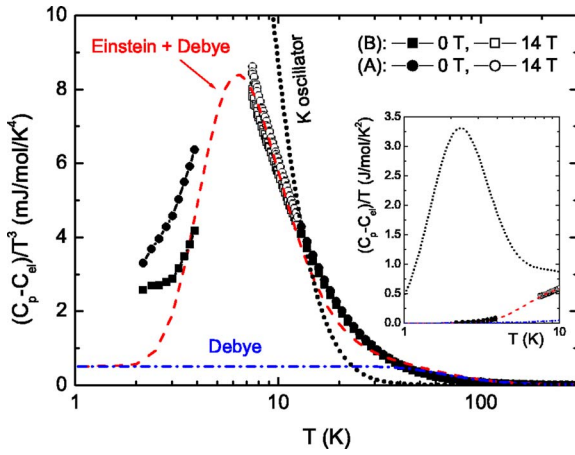


FIG. 8. (Color online) $(C_p - C_{el})/T^3$ of KOs_2O_6 on a logarithmic temperature scale. The dashed line shows a combined Einstein-Debye contribution with $n=0.15 \times 9$ modes/f.u., $T_E=31$ K, and $\Theta_D=325$ K to illustrate a best fit to the data if an Einstein-type contribution is assumed. We use the Debye temperature from RbOs_2O_6 (Fig. 7). The dotted line indicates the large lattice contribution expected at low temperatures from a K ion in an anharmonic potential (Ref. 32). The absence of such a contribution may indicate a freezing of the rattling motion at $T_{p,i}$. (A) and (B) refer to the two extrapolations used to extract γ as described in the main text.

tential being very anharmonic, leading to a vibrational spectrum that is not simply modeled by an Einstein mode. Nevertheless, we show a best fit of an Einstein contribution to the data in the figure, resulting in $n=0.15 \times 9$ modes/f.u. and $T_E=31$ K. For the Debye contribution which is expected to result mainly from the rigid Os-O network we have reused the Debye temperature from RbOs_2O_6 . The question about the low-energy lattice dynamics appears to be central to the physics of KOs_2O_6 . The calculated anharmonic potential for the K ion results in a set of discrete vibrational energies, leading to a distinct T dependence of the specific heat.³² The data deviate markedly from this model calculation at low temperature (Fig. 8). Possibly, this indicates a freezing of the dynamic motion of the alkali-metal ion.

F. Resistivity

As has been noted before,⁴ the resistivity of KOs_2O_6 shows a peculiar downward curvature, which extends to the lowest measured temperatures. This downward curvature also exists in the other AOs_2O_6 compounds, though at different temperatures: the curve looks like an additional hump superimposed on a more smooth background, the hump having its peak at a temperature shifting systematically to higher temperatures on going from $A=\text{K}$ to Cs . We analyze this behavior by taking the derivative of the resistivity with respect to temperature and then locating the maximum of the resulting curve. Owing to varying effective geometric factors due to grain sizes, the absolute values of the resistivities among samples vary significantly. In Fig. 9 we therefore show the normalized derivative of the resistivity where we have set the peak value to unity.

For illustrative purposes, we compare these results with a model calculation for the resistivity caused by an Einstein phonon³³

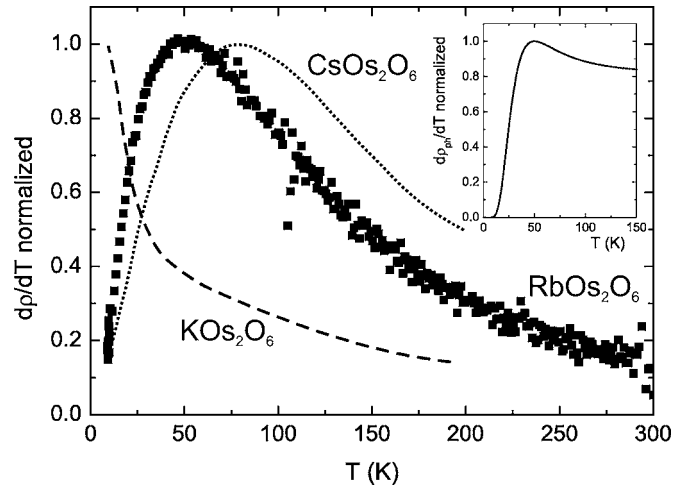


FIG. 9. Temperature derivative of the electrical resistivity $d\rho/dT$ normalized to the value at its maximum showing the systematic variation of the peak location with the A ion. The data for CsOs_2O_6 (dotted curve) and KOs_2O_6 (dashed curve) are taken from Refs. 11 and 4, respectively. The two curves are smoothed. The inset shows the calculation for a single Einstein phonon.

$$\rho_{\text{ph}} = \frac{2\pi m^* \alpha^2 F_E}{ne^2} \frac{\coth(T_E/2T)}{1 + 2/3 \sinh^2(T_E/2T)}, \quad (1)$$

where m^* is the averaged band mass, $\alpha^2 F_E$ is an Einstein spectral function, n is the number of conduction electrons per unit volume, e is the elementary charge, and $k_B T_E$ is the energy of the Einstein mode. The inset of Fig. 9 shows the derivative of the model resistivity for a peak at 50 K. It describes the data well at low temperatures, but deviates at higher temperatures, where the model predicts a resistivity linear in T .

The resulting temperatures T_{peak} at which $d\rho/dT$ peaks are plotted in Fig. 10 versus T_{Einstein} , the energy of the Einstein phonon mode extracted from the heat capacity measurement. $T_{\text{Einstein}} \approx 70$ K for CsOs_2O_6 is taken from Refs. 10 and 34. It can be shown that the derivative of the model resistivity $d\rho_{\text{ph}}/dT$ shows a maximum at $T_{\text{peak}} = T_E/a$, where $a \approx 2.243$.⁴³ For illustrative purposes, this line is shown along the experimental results from AOs_2O_6 in Fig. 10. As one might expect, this simple Einstein phonon model is not sufficient to describe the entire $\rho(T)$ curves, because scattering at other phonons is not included. If a second phonon is considered and the resulting resistivity is assumed to be simply the sum of the two single-phonon results according to Matthiessen's rule, then the location of the peak moves more toward the measured points: in an analysis of the specific heat data, Hiroi *et al.*^{10,34} have explained their data using a second phonon at around 140 K for RbOs_2O_6 and around 175 K for CsOs_2O_6 . Including a phonon at these temperatures moves the peak location up in temperature to 51 K for RbOs_2O_6 and 64 K for CsOs_2O_6 , shown by (blue) stars and arrows in Fig. 10. The deviation of the CsOs_2O_6 T_{peak} toward even higher temperatures may be due to the fact that at these temperatures a significant contribution to the phonon spectrum already stems from the Debye phonons neglected up to

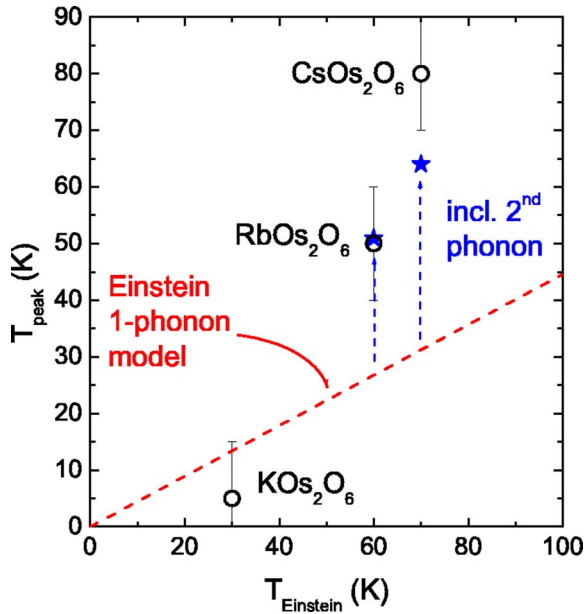


FIG. 10. (Color online) Systematic variation with the A ion of the maximum in the temperature derivative of the resistivity T_{peak} versus the characteristic temperature of the low-energy phonon T_{Einstein} extracted from heat capacity measurements. For illustration we show where the maxima are expected to lie according to the solution of the linearized Boltzmann equation for a single phonon by a dashed line (Ref. 33). Inclusion of a second phonon by Matthiessen's rule at around 140 K for RbOs_2O_6 and around 175 K for CsOs_2O_6 (Refs. 10 and 34) moves the peak temperature up toward the measured value shown by the (blue) stars and arrows.

now in the transport model. The overall trend, however, is well represented by such an analysis and it points to the significant scattering by the A atoms.

IV. DISCUSSION

The systematic variation of the position of the maximum slope in the resistivity indicates a close connection between the dynamics of the alkali-metal ion A and the electronic transport properties. KOs_2O_6 is somewhat different from the other two compounds, because its peak temperature is lower than expected from the simple Einstein phonon model (Fig. 10). This might be a result of the strong anharmonicity of the cage potential. It is known that the alkali-metal ions move in a strongly anharmonic potential and couple to the conduction electrons owing to their large excursion from equilibrium, and previous results have been interpreted in this scenario.^{10,34} This results in the electron-phonon coupling parameter λ_{ep} increasing, driving KOs_2O_6 more toward the strong-coupling regime. Electron scattering from the alkali-metal mode as the reason for the downward curvature of the resistivity has been suggested before by Kuneš *et al.*²² While the scattering at phonons seems to be the most plausible mechanism at this point, other scenarios for the peculiar behavior of the resistivity are also conceivable: Fermi surface nesting has been found in KOs_2O_6 and has been proposed as the driving force for strong spin fluctuations.³⁵ It remains to

be worked out in detail to what degree such fluctuations or even more exotic excitations could account for the measured resistivity. We note, however, that the static susceptibility of KOs_2O_6 is not significantly enhanced; rather it is smaller than expected based on the band density of states.

In the following we try to identify the various contributions to the measured mass enhancement reflected in the Sommerfeld coefficient γ . It is known that Coulomb and electron-phonon effects in a metal can be combined in a multiplicative fashion.³⁶ An interpretation of the additional enhancement in terms of Coulomb correlations would therefore mean a parametrization according to $1+\lambda=(1+\lambda_{\text{ep}})(1+\lambda_{\text{c}})$. In this interpretation the overall bandwidth is reduced by a factor of $1+\lambda_{\text{c}}$ due to electron-electron interactions. The resulting Coulomb enhancement parameter λ_{c} for RbOs_2O_6 is ≈ 1.0 and for KOs_2O_6 it is ≈ 1.7 {4.3}, from which we estimate the interaction strength: assuming a conduction electron density of $n=2$ electrons per Os, we can make a crude estimate of the Coulomb interaction potential: $V_{\text{c}}=n\lambda_{\text{c}}/N(0)\approx 2$ eV for RbOs_2O_6 and 3 eV {9 eV} for KOs_2O_6 . Here, $N(0)=g(E_{\text{F}})/2$ is the density of states at the Fermi level for one spin direction. Both of these values indicate a large electron correlation.

It is instructive to compare the AOs_2O_6 series with a Ru-based α -pyrochlore series, where variations of the Ru-O-Ru angle results in a drastic change of the density of states. The compound $\text{Y}_{2-x}\text{Bi}_x\text{Ru}_2\text{O}_7$ is a Mott insulator for small x and a normal paramagnetic metal for $x\approx 2$. The band Sommerfeld coefficient of $\text{Bi}_2\text{Ru}_2\text{O}_7$ is calculated to be 8.0 mJ/mol K²,³⁷ resulting in a very small mass enhancement ($\lambda\approx 0.23$). The correlations increase upon Y substitution resulting in an increase of the Sommerfeld coefficient from about 10 mJ/mol K² at $x\approx 2$ to almost 90 mJ/mol K² at $x\approx 0.9$.³⁸ The enhancement at $x=0.9$ is thus substantial: $\lambda\approx 10$. Below this critical value correlations become so strong that a gap opens in the density of states and the Sommerfeld coefficient decreases rapidly and vanishes in the Mott insulating state. Using the same arguments as above for AOs_2O_6 , the interaction potential V_{c} in $\text{Y}_{1.1}\text{Bi}_{0.9}\text{Ru}_2\text{O}_7$ is of the order of 10 eV, certainly large enough to cause a gap for a bandwidth of typically 3 eV. At the same time the Ru-O-Ru angle is reduced from about 139° for $\text{Bi}_2\text{Ru}_2\text{O}_7$ to 129° for $\text{Y}_2\text{Ru}_2\text{O}_7$.³⁹ This strongly indicates that a decreasing B-O-B angle causes the band to narrow and the correlations among conduction electrons to increase. AOs_2O_6 shows the same tendency: the Os-O-Os angle in RbOs_2O_6 is 139.4° ($\gamma=44$ mJ/mol K²), while that for KOs_2O_6 is 137.9° ($\gamma=76$ –110 mJ/mol K²). We thus interpret the mass of AOs_2O_6 to be increasingly enhanced by electron correlations going from A=Cs to A=K. Possibly the correlations are especially strong in some subband, leading to a charge-density-wave-like or orbitally ordered state at around 7 K ($T_{\text{p},1}$ and $T_{\text{p},2}$ in Fig. 3).

This is consistent with another series of pyrochlores: according to Solovyev,⁴⁰ a decreasing Mo-O-Mo angle in $\text{R}_2\text{Mo}_2\text{O}_7$ reduces the interaction between $\text{Mo}(t_{2g})$ orbitals which is mediated by $\text{O}(2p)$ states, causing diminishing overlap and thus enhanced mass. Although this author finds the lattice parameter to be the relevant parameter determin-

ing the physics of the compound, the physical properties of various pyrochlores appear to be more appropriately parametrized by the metal-oxygen-metal angle.

An effective Hubbard U of 2 eV is in line with other transition metals. According to Ref. 28, this is not enough to classify $\text{Cd}_2\text{Os}_2\text{O}_7$ as a strongly correlated system. In Ref. 40, however, a U of 1.5–2.5 eV explains the Mott-insulating properties of $\text{R}_2\text{Mo}_2\text{O}_7$ very well. This might be a somewhat weak argument, because $\text{Cd}_2\text{Os}_2\text{O}_7$ is a $5d$ material while $\text{R}_2\text{Mo}_2\text{O}_7$ is $4d$, which are usually more strongly correlated. On the other hand, the LDA bandwidth of AOs_2O_6 is in the region of $W \approx 3$ eV,^{22,35} and the interaction potential V_c is therefore comparable to W and thus the Mott-Hubbard localization concept is applicable. The anomalous pressure dependence of the superconducting transition temperature is in line with these findings:⁴¹ Hydrostatic pressure reduces the correlations working against superconductivity, thus initially increasing the critical temperature. For this reason it would be of interest to see if NaOs_2O_6 shows metallic or insulating behavior.

It is enlightening to compare the electronic structure of AOs_2O_6 to the one of OsO_2 , since, in a (limited) way, OsO_2 can be regarded as AOs_2O_6 without the A . It has a rutile structure with the OsO_6 octahedra sharing edges in the c direction and corners in the plane perpendicular to c .⁴² While the Os-Os distance to the neighboring octahedron with the shared edge and the length of the shared edge itself are shorter than the Os-Os and O-O distances in AOs_2O_6 , all other Os-O, O-O, and Os-Os distances in OsO_2 are slightly longer than the ones in AOs_2O_6 . The Os-O-Os angles in OsO_2 are 105.0° along the c axis and 127.5° perpendicular to it. Pyrochlores with a $B\text{-O-B}$ angle around 127° usually are in an insulating state. Directional resistivity measurements on OsO_2 could thus be quite insightful in this respect.

The density of states at the Fermi level for OsO_2 of about 13–15 states/unit cell Ry spin from the band structure calculation in Ref. 42 results in a Sommerfeld coefficient $\gamma_b \approx 2.4$ mJ/mol K². We measure a γ of about 6.1 mJ/mol K², resulting in a specific heat enhancement of about $1 + \lambda = 6.1/2.4 \approx 2.5$. Assuming a small electron-phonon coupling in OsO_2 of $\lambda_{\text{ep}} \approx 0.2$ and an enhancement of the form $\gamma/\gamma_b = (1 + \lambda_{\text{ep}})(1 + \lambda_c)$, this results in an enhancement due to correlations of $\lambda_c \approx 1.1$. This is quite a large enhancement parameter similar to the one of AOs_2O_6 , providing further evidence that the Coulomb correlations are inherent to the Os-O system.

Recent calculations have shown that the electronic structure does not change significantly on changing the alkali-metal ion A .²⁵ Therefore, all these considerations point to the need to consider interactions that are not captured in the electronic structure calculations. In light of the significant electron-phonon interaction, and even stronger effects due to electron correlations, it will be of interest to further focus on

the possible role played by the three-dimensional triangular geometry of the Os-O network. In view of the strong electron correlations, the frustrated geometry might be of importance in these materials.

We take the nonsuperconducting state of $\text{Y}_{2-x}\text{Bi}_x\text{Ru}_2\text{O}_7$ to be a clear indication that the additional enhancement mechanism is to be regarded separately from the pairing mechanism. Both AOs_2O_6 and $\text{Y}_{2-x}\text{Bi}_x\text{Ru}_2\text{O}_7$ show significant enhancement due to correlations, but only AOs_2O_6 is superconducting. The question thus remains why AOs_2O_6 is superconducting and $\text{Y}_{2-x}\text{Bi}_x\text{Ru}_2\text{O}_7$ is not. The answer may lie in the electron-phonon coupling, which is unusually large in AOs_2O_6 . We expect this to be due to the β -pyrochlore instead of the α -pyrochlore structure, which leaves the $16d$ site empty and the $8b$ site occupied by A instead of an oxygen atom. This should significantly modify the phonon spectrum, resulting in a large λ_{ep} .

V. CONCLUSION

Our data from high-quality single-crystalline KOs_2O_6 show that KOs_2O_6 is a particularly interesting transition metal oxide: it is an intermediate- to strong-coupling type-II superconductor with a coupling parameter $\lambda_{\text{ep}} \approx 1\text{--}1.6$. KOs_2O_6 has a high Sommerfeld coefficient for a pyrochlore of 76–110 mJ/mol K². We estimate a Ginzburg-Landau coherence length $\xi \approx 31\text{--}37$ Å, about half the one in RbOs_2O_6 due to the renormalization of the Fermi velocity v_F . We estimate the condensation energy $-\Delta F = 2.0\text{--}2.5$ J/mol. The effective mass, even after the measured strong electron-phonon renormalization is taken into account, is threefold enhanced over the LDA band mass. We interpret this as due to Coulomb correlations. The renormalization affects those electrons that are paired to form the superconducting condensate. While for RbOs_2O_6 the additional heat capacity can be well characterized by an Einstein model, the contribution for KOs_2O_6 is somewhat more unusual, possibly due to strong anharmonicity. We associate this special phonon with a rattling motion of the alkali-metal ions, resulting in three modes per Rb for RbOs_2O_6 . In KOs_2O_6 , the absence of lattice heat capacity at low temperatures may indicate the freezing of this motion. The dynamics of the alkali-metal ions causes large scattering of the charge carriers which shows up in an unusual temperature dependence of the electrical resistivity which varies systematically with the alkali-metal ion.

ACKNOWLEDGMENTS

We thank J. Kuneš and W. E. Pickett for helpful discussions on the calculation of the lattice vibrational spectrum and R. Saniz for providing revised values for the Fermi velocities. This study was partly supported by the Swiss National Science Foundation.

*Electronic address: markus.bruehwiler@phys.ethz.ch

- ¹R. Moessner, *Can. J. Phys.* **79**, 1283 (2001).
- ²J. E. Greedan, *J. Mater. Chem.* **11**, 37 (2001).
- ³A. P. Ramirez, *Annu. Rev. Mater. Sci.* **24**, 453 (1994).
- ⁴S. Yonezawa, Y. Muraoka, Y. Matsushita, and Z. Hiroi, *J. Phys.: Condens. Matter* **16**, L9 (2004).
- ⁵P. W. Anderson, *Mater. Res. Bull.* **8**, 153 (1973).
- ⁶M. Hanawa, Y. Muraoka, T. Tayama, T. Sakakibara, J. Yamaura, and Z. Hiroi, *Phys. Rev. Lett.* **87**, 187001 (2001).
- ⁷H. Sakai, K. Yoshimura, H. Ohno, H. Kato, S. Kambe, R. E. Walstedt, T. D. Matsuda, Y. Haga, and Y. Onuki, *J. Phys.: Condens. Matter* **13**, L785 (2001).
- ⁸R. Jin, J. He, S. McCall, C. S. Alexander, F. Drymiotis, and D. Mandrus, *Phys. Rev. B* **64**, 180503(R) (2001).
- ⁹S. Yonezawa, Y. Muraoka, Y. Matsushita, and Z. Hiroi, *J. Phys. Soc. Jpn.* **73**, 819 (2004).
- ¹⁰Z. Hiroi, S. Yonezawa, J.-I. Yamaura, T. Muramatsu, Y. Matsushita, and Y. Muraoka, *J. Phys. Soc. Jpn.* **74**, 3400 (2005).
- ¹¹S. Yonezawa, Y. Muraoka, and Z. Hiroi, *J. Phys. Soc. Jpn.* **73**, 1655 (2004).
- ¹²M. Brühwiler, S. M. Kazakov, N. D. Zhigadlo, J. Karpinski, and B. Batlogg, *Phys. Rev. B* **70**, 020503(R) (2004).
- ¹³R. Khasanov *et al.*, *Phys. Rev. Lett.* **93**, 157004 (2004).
- ¹⁴K. Magishi, J. L. Gavilano, B. Pedrini, J. Hinderer, M. Weller, H. R. Ott, S. M. Kazakov, and J. Karpinski, *Phys. Rev. B* **71**, 024524 (2005).
- ¹⁵M. Brühwiler, S. M. Kazakov, J. Karpinski, and B. Batlogg, *Phys. Rev. B* **71**, 214517 (2005).
- ¹⁶S. Manalo, H. Michor, G. Hilscher, M. Brühwiler, and B. Batlogg (unpublished).
- ¹⁷A. Koda, W. Higemoto, K. Ohishi, S. R. Saha, R. Kadono, S. Yonezawa, Y. Muraoka, and Z. Hiroi, *J. Phys. Soc. Jpn.* **74**, 1678 (2005).
- ¹⁸G. Schuck, S. M. Kazakov, K. Rogacki, N. D. Zhigadlo, and J. Karpinski, *cond-mat/0601465* (unpublished).
- ¹⁹S. M. Kazakov, N. D. Zhigadlo, M. Brühwiler, B. Batlogg, and J. Karpinski, *Semicond. Sci. Technol.* **17**, 1169 (2004).
- ²⁰Z. Hiroi, S. Yonezawa, J.-I. Yamaura, T. Muramatsu, and Y. Muraoka, *J. Phys. Soc. Jpn.* **74**, 1682 (2005).
- ²¹R. Saniz (private communication).
- ²²J. Kunes, T. Jeong, and W. E. Pickett, *Phys. Rev. B* **70**, 174510 (2004).
- ²³G. E. Volovik, *JETP Lett.* **58**, 469 (1993).
- ²⁴F. Marsiglio, J. M. Coombes, and J. P. Carbotte, *Phys. Rev. B* **35**, 3219 (1987).
- ²⁵R. Saniz and A. J. Freeman, *Phys. Rev. B* **72**, 024522 (2005).
- ²⁶D. J. Singh, *Phys. Rev. B* **52**, 1358 (1995).
- ²⁷T. Oguchi, *Phys. Rev. B* **51**, 1385 (1995).
- ²⁸D. J. Singh, P. Blaha, K. Schwarz, and J. O. Sofo, *Phys. Rev. B* **65**, 155109 (2002).
- ²⁹K. Arai, J. Kikuchi, K. Kodama, M. Takigawa, S. Yonezawa, Y. Muraoka, and Z. Hiroi, *cond-mat/0411460* (unpublished).
- ³⁰F. Marsiglio and J. P. Carbotte, *Phys. Rev. B* **33**, 6141 (1986).
- ³¹R. G. Chambers, *Proc. Phys. Soc. London* **78**, 941 (1961).
- ³²J. Kunes and W. E. Pickett, *Physica B* (to be published), <http://dx.doi.org/10.1016/j.physb.2006.01.491>
- ³³H.-L. Engquist, *Phys. Rev. B* **21**, 2067 (1980).
- ³⁴Z. Hiroi, S. Yonezawa, T. Muramatsu, J.-I. Yamaura, and Y. Muraoka, *J. Phys. Soc. Jpn.* **74**, 1255 (2005).
- ³⁵R. Saniz, J. E. Medvedeva, L.-H. Ye, T. Shishidou, and A. J. Freeman, *Phys. Rev. B* **70**, 100505(R) (2004).
- ³⁶R. E. Prange and A. Sachs, *Phys. Rev.* **158**, 672 (1967).
- ³⁷F. Ishii and T. Oguchi, *J. Phys. Soc. Jpn.* **69**, 526 (2000).
- ³⁸S. Yoshii and M. Sato, *J. Phys. Soc. Jpn.* **68**, 3034 (1999).
- ³⁹R. Kanno, Y. Takeda, T. Yamamoto, Y. Kawamoto, and O. Yamamoto, *J. Solid State Chem.* **102**, 106 (1993).
- ⁴⁰I. V. Solov'yev, *Phys. Rev. B* **67**, 174406 (2003).
- ⁴¹T. Muramatsu, N. Takeshita, C. Terakura, H. Takagi, Y. Tokura, S. Yonezawa, Y. Muraoka, and Z. Hiroi, *Phys. Rev. Lett.* **95**, 167004 (2005).
- ⁴²L. F. Mattheiss, *Phys. Rev. B* **13**, 2433 (1976).
- ⁴³ a is the nonzero solution of $2 \sinh(a/2) + 5a \cosh(a/2) - 18a \cosh^3(a/2) + 16 \sinh(a/2) \cosh^6(a/2) - 8a \cosh^7(a/2) + 12a \cosh^5(a/2) = 0$.